electronics

MDPI

Article

Cyanate Ester–Lunar Regolith Composites for In Situ Fabrication of Structural Electronics on the Moon

Guancheng Li [1], Batuhan Mirac Alasahin [2], Mark Mirotznik [2,*] and Robert L. Opila [1,*]

[1] Department of Materials Science and Engineering, University of Delaware, Newark, DE 19716, USA; guanchl@udel.edu
[2] Department of Electrical and Computer Engineering, University of Delaware, Newark, DE 19716, USA; batu@udel.edu
* Correspondence: mirotzni@udel.edu (M.M.); opila@udel.edu (R.L.O.)

Abstract

The development of electronic substrates from locally available materials is critical for sustainable lunar infrastructure. This work investigates the synthesis, processing, and characterization of cyanate ester–lunar regolith simulant (CE-LRS) composites designed specifically for the extreme lunar environment. LRS were evaluated as functional fillers at loadings up to 55 wt.% with CE binder selected for its thermal stability (T_g > 230 °C), vacuum compatibility, and known radiation resistance from prior literature. A vacuum-assisted curing procedure was developed that utilizes the lunar environment as a processing advantage, reducing porosity from approximately 7% to less than 1% as quantified by X-ray micro-computed tomography. Dynamic mechanical analysis revealed that increased filler loading and vacuum processing enhanced the storage modulus and T_g through constraining polymer chain mobility at the filler-binder interface, confirming effective stress transfer and interfacial adhesion. Scanning electron microscopy also verified intimate polymer–filler wetting. Waveguide measurements in the microwave frequency range demonstrated that the composites remain non-magnetic while exhibiting moderately increased permittivity and low dielectric loss, meeting the requirements for radio-frequency substrate applications. Through material selection and process design that embraces, rather than ignores, lunar environmental constraints, this work establishes the CE-LRS composites that represent a viable pathway for the in situ fabrication of structural electronics on the Moon.

Keywords: printed wiring board; regolith simulant; cyanate ester; porosity; dielectric loss; permittivity

Check for updates

Academic Editor: Elias Stathatos

Received: 3 April 2026
Revised: 4 May 2026
Accepted: 14 May 2026
Published: 20 May 2026

Copyright: © 2026 by the authors. Licensee MDPI, Basel, Switzerland. This article is an open access article distributed under the terms and conditions of the Creative Commons Attribution (CC BY) license.

1. Introduction

Establishing sustainable capabilities for lunar and deep space exploration necessitates a shift from Earth-dependent logistics toward advanced in situ resource utilization (ISRU). The use of lunar regolith is important for this transition. However, the demanding lunar environment, including temperature changes ranging over 300 °C between day and night and an ultra-high vacuum that induces material outgassing, poses significant challenges for engineering systems. As presented in reviews by Suhaizan et al. and Ince et al. [1,2], the last decade has shown an increase in research focused on consolidating regolith simulants into solid materials. While efforts have focused on using regolith for bulk construction and radiation shielding [3–5], the in situ fabrication of functional components, particularly robust electronic devices, remains a challenge for long-term mission self-sufficiency.

The ability to manufacture wiring boards and structural electronics on extraterrestrial surfaces would reduce payload. Conventional solutions are inadequate. Existing utilization strategies for regolith, such as sintering or geopolymerization, often result in brittle ceramics with limited thermo-mechanical properties for electronic applications [2,6–9]. On the other hand, the standard substrates, like FR-4 laminates, are not suited for space. Their polymer matrices can outgas in vacuum, contaminating optics and sensors [10]. Also, their lower glass transition temperatures (T_g) risk structural failure during thermal cycling [11].

A potential pathway lies in the development of polymer–regolith composites, which combines the functional and processing advantages of polymers and the in situ availability of lunar soil. The selection of the polymer binder is critical. It should withstand the lunar environment. Prior work has demonstrated this concept (shown in Table 1). For example, Matetich and Vold [12] fabricated Martian regolith–polypropylene composites using conventional manufacturing techniques such as twin-screw extrusion and injection molding. Jakus et al. [13] and Taylor et al. [14] developed extrudable regolith inks incorporating bio-derived and synthetic polymers to print complex structures. Despite these advances, as mentioned in the review by Ince et al. [1], most of these polymer systems are designed for processability rather than environmental resilience. Their limited thermal stability and potential to outgas under vacuum show risks for long-term missions.

Table 1. Comparison of existing polymer–regolith systems and their limitations relative to lunar environmental requirements.

Polymer System	T_g (°C)	Vacuum Outgassing	Limitation for Lunar Electronics
PP [12]	<30	Low	Low T_g
PLGA [13,14]	<50	Moderate	Low T_g, residual solvents release risk
CE (this work)	210	Low	Meets requirements

Note: PP (polypropylene); PLGA (polylactic-co-glycolic acid).

Our work addresses this gap by employing cyanate ester resins, a class of high-performance polymers selected from their known high T_g, vacuum compatibility, and radiation resistance from prior literature [15–19]. We present a comprehensive characterization of the cyanate ester–lunar regolith simulant, CE-LRS, composite, demonstrating its viability through thermal analysis, microstructural examination, mechanical testing, and electromagnetic property evaluation. Our results confirm that the vacuum-processed CE-LRS composite achieves low porosity, high stiffness, and non-magnetic properties suitable for wiring board applications, advancing the feasibility of ISRU for electronics.

2. Experimental

2.1. Materials

The LRS used in this study was OPRH4W30 (lunar highland simulant), provided by John E. Gruener at NASA Johnson Space Center (JSC) in Houston, TX, USA. The primary polymer matrix was a proprietary CE resin system, APC6.51.2 Part A&B (Patz Materials & Technologies, Benicia, CA, USA), consisting of Part A (cyanate ester monomer) and Part B (catalyst), mixed at a Part B ratio of 6.7%. APC6.51.2 comprises a blend of cyanate ester resins with varying viscosities, engineered to optimize compatibility with high loadings of fillers and additives.

2.2. Preparation of Regolith–Polymer Composites

The LRS powder was sieved to a particle size below 106 μm prior to use if not otherwise specified. The CE composite ink was prepared by mixing the LRS powder with the CE

resin (Part A) and catalyst (Part B). For a standard formulation, 2.0 g of LRS powder was mixed with 1.64 g of CE resin system, resulting in an ink with 55 wt% solid loading of LRS.

The ink was then poured into a rectangular mold of 0.9 × 0.4 inches (22.86 × 10.16 mm) made of Aluminum 2024. Two curing procedures were employed. For the ambient pressure curing, the filled mold was directly transferred to an oven. For the vacuum-assisted curing, the idea was to simulate the environment on the moon. The LRS was pre-baked under 200 °C for an hour before mixing to remove any possibly existing water and hydroxyl group on the surface. After pouring into the mold, the ink was subjected to a degassing process using a rough vacuum pump to remove entrapped air before transferring to the oven. For both procedures, the thermal cycle was identical: the temperature was ramped from 55 °C to 120 °C at a rate of 0.3 °C per minute, followed by an isothermal hold at 120 °C for 8 h to ensure complete curing. After curing, the samples were cooled slowly to room temperature inside the oven before demolding.

Since the purpose of this work was to demonstrate the formulation of regolith/CE composites, only one specimen was made at each composition. Thus, there is no statistical data for any of the characterizations.

2.3. Characterization Techniques

Differential Scanning Calorimetry (DSC): A NETZSCH DSC 214 Polyma (NETZSCH-Gerätebau GmbH, Selb, Germany), was used. The cure behavior of the CE resin was analyzed by heating from −50 °C to 250 °C at 5 °C/min under nitrogen, while the fully cured CE was measured by heating from room temperature to 250 °C at the same rate to obtain T_g. For the CE-LRS composite mixtures (with 20 wt% and 55 wt% LRS loading), the scans were initiated from 85 °C to 250 °C at 5 °C/min to focus on the curing exotherm and temperature. All reported data were obtained from heating data. The results of uncured samples are from the first heating cycle, and the cured ones are from the second heating cycle.

Scanning Electron Microscopy (SEM): A Carl Zeiss Auriga 60 CrossBeam SEM (Carl Zeiss Microscopy GmbH, Jena, Germany) was used to examine raw LRS powders and composite fracture surfaces. The samples were sputter-coated with gold prior to imaging. Energy-dispersive X-ray spectroscopy (EDS) was used for elemental mapping.

X-Ray Micro-Computed Tomography (Micro-CT): The porosity and internal structure of the cured composite samples were analyzed using a Rigaku GX 130 CT Scanner micro-CT system (Rigaku Corporation, Tokyo, Japan). The 3D reconstructions were used to quantify the porosity difference between samples cured with and without the vacuum-assisted step.

Dynamic Mechanical Analysis (DMA): A NETZSCH EPLEXOR® analyzer (NETZSCH-Gerätebau GmbH, Selb, Germany) equipped with a 150 N force sensor was used to evaluate the viscoelastic response of the cured CE resin and CE-LRS composites. Measurements were performed in three-point bending mode with a 20 mm support span on cuboid specimens with nominal dimensions of 10 mm × 2.5–3.2 mm (width × thickness). Temperature sweeps were conducted from 25 °C to 180 °C at a heating rate of 2.0 K/min and a step width of 1.0 °C, yielding 156 measurement points per scan. A sinusoidal dynamic force of 2.50 N was applied at a frequency of 1.00 Hz and a static load of 7.00 N, with a contact force of 1.00 N and a strain limit set to 50% of the specimen thickness.

The electromagnetic properties of the cured CE-LRS composites were measured in the X-band frequency range of 8.2–12.4 GHz using a rectangular waveguide method. Scattering parameters were collected with an Agilent Technologies E8361C vector network analyzer (Agilent Technologies, Santa Clara, CA, USA) after through-reflect-line calibration using a Flann Microwave calibration kit (Flann Microwave Ltd., Bodmin, Cornwall, UK). The complex permittivity and permeability were extracted from the measured S-parameters

using the Nicolson–Ross–Weir algorithm. The samples were prepared with dimensions of 22.86 × 10.16 mm, corresponding to the WR-90 waveguide aperture, to minimize residual air gaps between the specimen and waveguide walls during measurement.

3. Results and Discussion

3.1. Thermal Properties

The thermal behavior of the cyanate ester (CE) resin and its composites with LRS is primarily examining their suitability for lunar manufacturing and operation. The lunar surface temperature environment, which varies from approximately −173 °C to 127 °C [20], demands a polymer matrix with thermal stability, characterized by a high T_g to prevent structural softening or failure during the lunar day.

Figure 1a presents the DSC thermograms of the CE resin before and after the curing process. The uncured resin (red line) exhibits a glass transition with a midpoint T_g of −32 °C, followed by a sharp exothermic peak with an onset temperature near 120 °C, corresponding to the thermally initiated cyclotrimerization reaction that forms the highly cross-linked polycyanurate network [21]. Because of the exothermicity of the reaction, the curing must be done slowly to limit the excess generation of heat and a concomitant runaway reaction. After curing (purple line), this exotherm is absent, confirming complete reaction. The cured material displays a high T_g of 231 °C, exceeding the maximum lunar surface temperature, confirming that the cured CE matrix will remain in its rigid state throughout the lunar temperature cycle, ensuring dimensional stability for electronic substrates. For comparison, typical polyimide substrates (e.g., Kapton®, Dupont, Wilmington, DE, USA) usually exhibit a T_g higher than 300 °C but are often processed as films rather than as composite matrices [22–24]. Bismaleimide (BMI) resins, commonly used in high-temperature printed circuit boards, have T_g values between 250 °C and 320 °C [25–27], depending on the formulation. While the CE resin's T_g (231 °C) is lower than many BMIs', it remains well above the lunar daytime maximum (127 °C) and offers advantages in dielectric properties [17,28]. Thus, CE-LRS composites provide a balanced combination of thermal stability and RF performance suitable for lunar structural electronics.

To evaluate the impact of LRS incorporation on the curing kinetics and to establish a processing window without thermal runaway, the curing behaviors of the uncured CE, CE-20%LRS, and CE-55%LRS mixtures were compared (Figure 1b). The introduction of LRS, even at a high loading of 55 wt%, does not significantly alter the onset or the peak temperature of the exotherm. This indicates that the LRS particles act primarily as an inert filler during the cure, not inhibiting or catalyzing the reaction. This consistency allows for a unified curing recipe for LRS at different weight fractions without burning during the exothermic reaction.

The DSC curve for a fully cured CE-55%LRS composite (Figure 1c) showed no residual exotherm. The composite retained a high T_g of approximately 230 °C, nearly identical to the neat resin. This demonstrates the curing profile's effectiveness and confirms the composite's thermal stability for lunar applications.

3.2. Microstructures and Porosity

3.2.1. Microstructure of LRS and the CE-LRS Composite

The microstructure of the raw materials and the quality of the polymer–filler interface are crucial to the composite's overall properties. Figure 2 presents SEM images and corresponding energy-dispersive X-ray spectroscopy (EDS) element distribution results of the LRS, OPRH4W30 (highland), after sieving to a particle size below 106 μm. The simulant exhibits the characteristic irregular, angular morphology expected of lunar regolith. The

elemental map confirms the complex silicate-based composition, showing a distribution of primary elements.

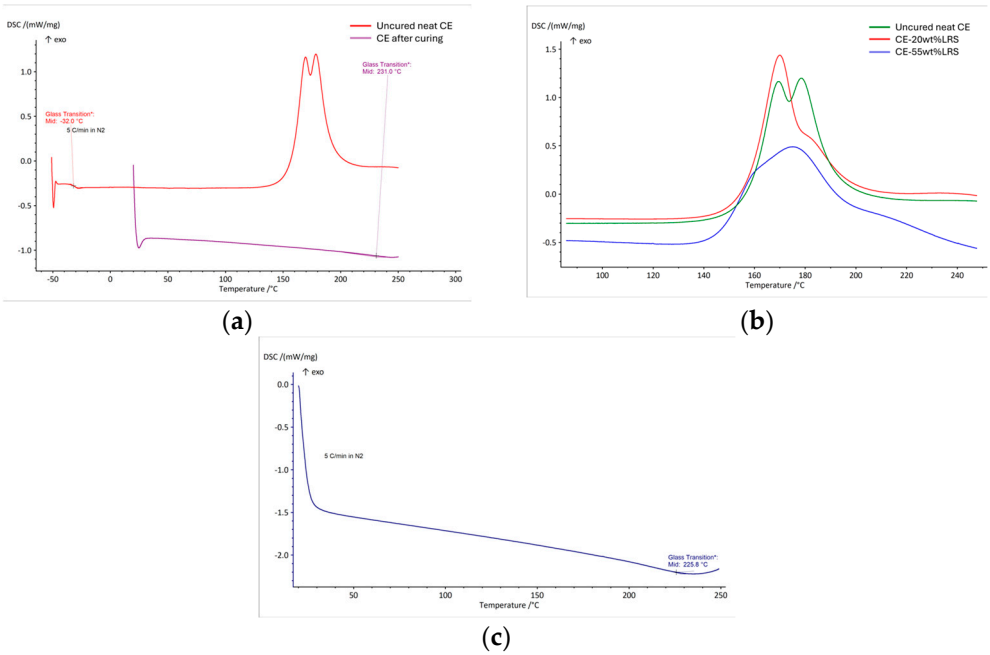


Figure 1. (**a**) DSC curves of neat cyanate ester (CE) resin before (red) and after (purple) curing. (**b**) Comparison of DSC curing exotherms for uncured neat CE (green), CE-20 wt% LRS (red), and CE-55 wt% LRS (blue) mixtures. (**c**) DSC curve for a fully cured CE-55%LRS composite. * The reported T_g is the midpoint of the transition.

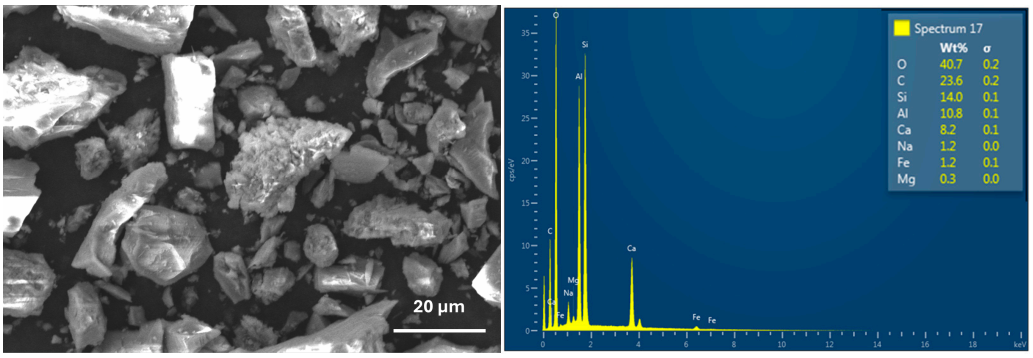


Figure 2. (**a**) SEM images (15 kV accelerating voltage, 8.4 mm working distance) and (**b**) corresponding EDS reports of the sieved (<106 µm) lunar regolith simulant OPRH4W30 (highland).

Figure 3a shows an SEM image of a fracture surface from a cured CE-55%LRS composite. The micrograph demonstrates the particle wetting property. The cyanate ester resin encapsulates the LRS particles, forming a continuous matrix with no visible voids at the interface, indicating strong adhesion. The EDS map (Figure 3b,c, red for carbon from the polymer and green for silicon from the regolith) would further illustrate this intimate contact. This dense, well-integrated microstructure is a prerequisite for achieving high stiffness.

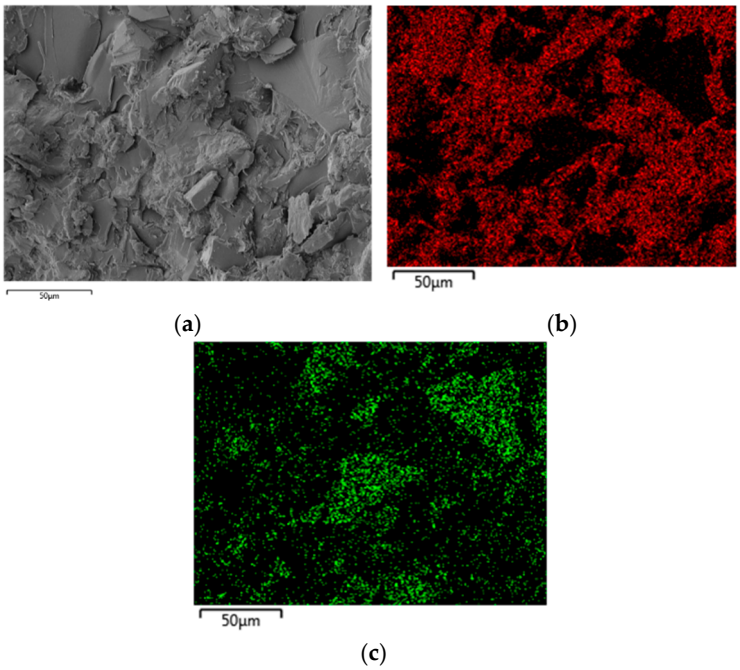


Figure 3. (**a**) SEM of the cured CE-55%LRS composite. (**b**,**c**) EDS elemental map of C (in red) and Si (in green), separately, illustrating the distinct but well-bonded interface between the polymer and the regolith particles. (5 kV accelerating volatage, 7.9 mm working distance).

3.2.2. Micro-CT and Porosity

The pore size and distribution within a composite directly influences its electromagnetic response. Porosity introduces air inclusions into the solid matrix, reducing the effective permittivity as described by classical dielectric mixing models. Moreover, pore–matrix interfaces act as scattering sites and sources of interfacial polarization, which can increase dielectric loss. Minimizing porosity is therefore critical for achieving low-loss dielectric performance in composite materials [29,30].

To observe the pore structure of the composites, X-ray micro-CT was performed on CE-55%LRS samples cured under two conditions: ambient pressure, representing Earth-based fabrication, and vacuum, representing the native lunar surface environment. Figure 4 presents representative cross-sectional slices from three vertical positions—top, middle, and bottom—through each sample, with pores highlighted in blue.

	Top	**Middle**	**Bottom**	**Porosity (%)**
Ambient Pressure				~7%
Vacuum				<1%

Figure 4. Representative X-ray micro-CT cross-sectional slices of CE-55%LRS composites cured under ambient pressure and vacuum conditions, taken from the top, middle, and bottom regions of each sample. Pores are highlighted in blue, while the composite material is shown in red.

The ambient pressure sample exhibits a heterogeneous porosity distribution, with the top region being relatively dense while the middle and bottom regions show progressively

larger and more numerous voids. In contrast, the vacuum-cured sample displays a nearly pore-free microstructure across all regions in the sample. Quantitative analysis confirmed that the vacuum-processed sample achieved an internal porosity of less than 1%. These results indicate that composites fabricated directly on the lunar surface would benefit from the vacuum, which naturally promotes degassing and yields denser microstructures than equivalent processing in the Earth's atmosphere.

3.3. Mechanical Properties

The effect of filler loading on the composite properties is governed by the characteristics of the interphase, which can be illustrated by dynamic mechanical analysis (DMA) [31]. Figure 5 presents the variation in the storage modulus (E′, a measure of the stored energy in a material during deformation) as a function of temperature for the CE and its composites filled with LRS at different weight fractions. The numerical values are presented in Table 2 for easier comparison.

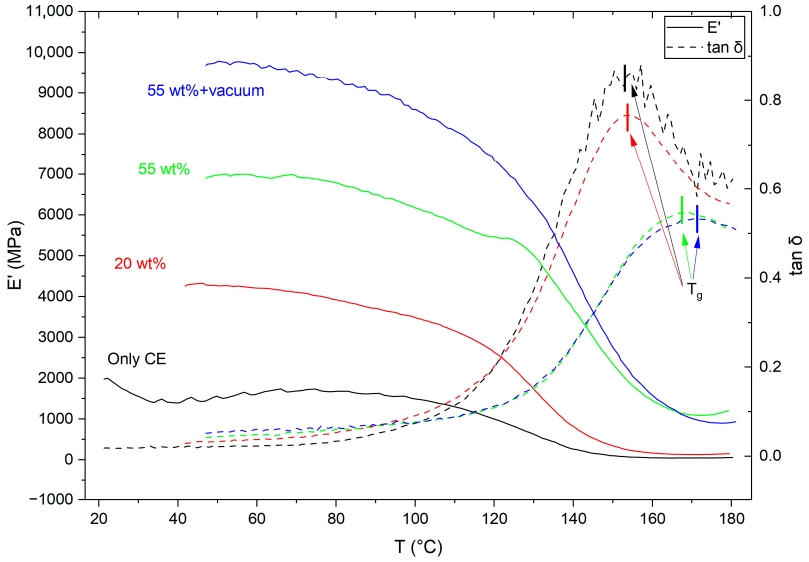


Figure 5. Storage modulus and tan δ results of CE filled with different weight fractions of LRS.

Table 2. Dynamic mechanical analysis results for CE-LRS composites.

Sample	E′ at 50 °C (GPa)	E′ at 150 °C (GPa)	Tan δ Peak Value	T_g from tan δ Peak (°C)	Percentage Increase in E′ at 50 °C
1 (Only CE)	1.56	0.10	0.87	153	/
2 (CE-20 wt% LRS)	4.26	0.34	0.77	154	173% compared with #1
3 (CE-55 wt% LRS)	6.98	2.33	0.55	169	374% compared with #1
4 (CE-55 wt% LRS with vacuum)	9.79	2.74	0.53	172	40% compared with #3

An obvious increase in the storage modulus is observed with the addition of LRS, confirming the expected reinforcement effect induced by the rigid filler particles. Notably, within the glassy state (temperatures significantly below the T_g), the composite containing 55 wt% LRS with additional vacuum processing exhibits a consistently higher storage modulus compared to the one without vacuum processing at the same loading. This enhancement is attributed to better interfacial adhesion achieved through vacuum processing. The removal of air and potential volatiles at the powder–polymer interface likely improves wetting and Van der Waals forces at the filler/polymer interface, leading to more efficient

stress transfer from the compliant polymer matrix to the rigid LRS particles. This behavior aligns with observations reported for compatibilized polymer blends where improved adhesion yields enhanced stiffness [32–34].

Figure 5 also presents the loss tangent (tan δ, the relative rate of energy dissipation or the damping of the material) change with temperature for the same set of composites. At temperatures far below the onset of the glass transition (below ~100 °C), all samples exhibit very low and similar tan δ values (<0.1). In this temperature range, polymer chains are frozen, and energy dissipation is minimal and primarily governed by localized, small-scale motions within the polymer itself.

As temperature increases, the polymer chain segments begin to acquire mobility, and change in behavior occurs. The tan δ of the unfilled CE (0 wt% LRS) and the 20 wt% LRS composite rises sharply. In contrast, both 55 wt% LRS composites (with and without vacuum processing) show a less steep rise in tan δ in this region, with nearly identical curve at this stage. This demonstrates that the higher filler loading creates a dense network of physical cross-links via filler–polymer interfacial interactions, which increase the volume of constrained polymer chains in the composites, thereby suppressing energy dissipation [35].

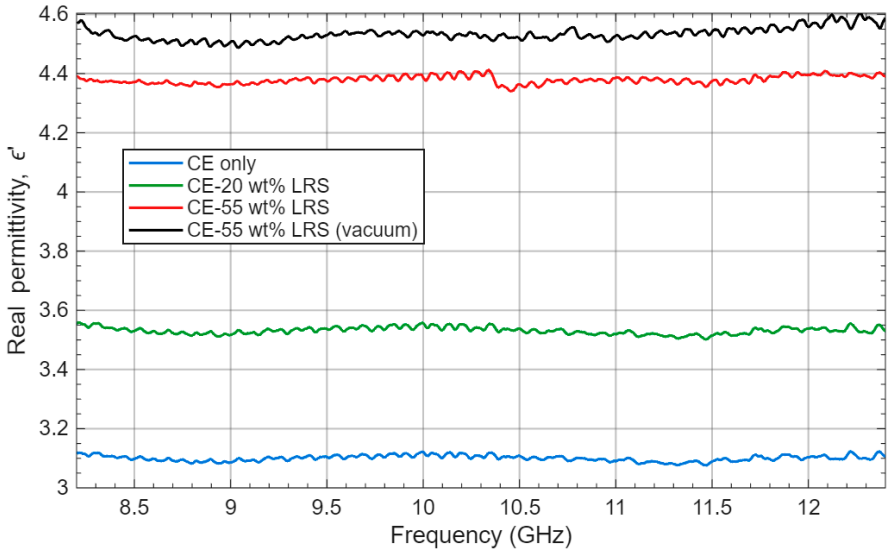
At the peak of the transition, both 55 wt% LRS composites have lower tan δ peak value and higher glass transition temperature, T_g, compared with the other two, and the vacuum-processed 55 wt% LRS composite exhibits a slightly lower tan δ peak value compared to the non-vacuum-processed 55 wt% LRS composite, while having similar but slightly higher T_g. The difference in T_g values confirms that both 55 wt% LRS composites impose a stronger constraint on the motion of polymer chains, increasing the temperature required for segmental relaxation compared to the unfilled polymer and 20 wt% LRS composite [36,37]. The reduction in tan δ peak values indicates the same conclusion [31]. The lower tan δ peak and slightly higher T_g for the vacuum-processed sample also indicated a stronger, more uniform interface [36] compared with the one without vacuum treatment that likely has interfaces with slightly weaker adhesion or more micro-defects.

In summary, the incorporation of LRS filler improves the mechanical properties of the CE matrix. The application of vacuum processing during composite fabrication enhances this effect by promoting interfacial adhesion. This is demonstrated not only by increased stiffness but also by a more favorable damping factor (tan δ). These findings confirm the strong interfacial interactions between the CE matrix and the LRS. This also validates the strategy of increasing regolith content within a reasonable range to enhance the thermo-mechanical performance of LRS-CE composites.

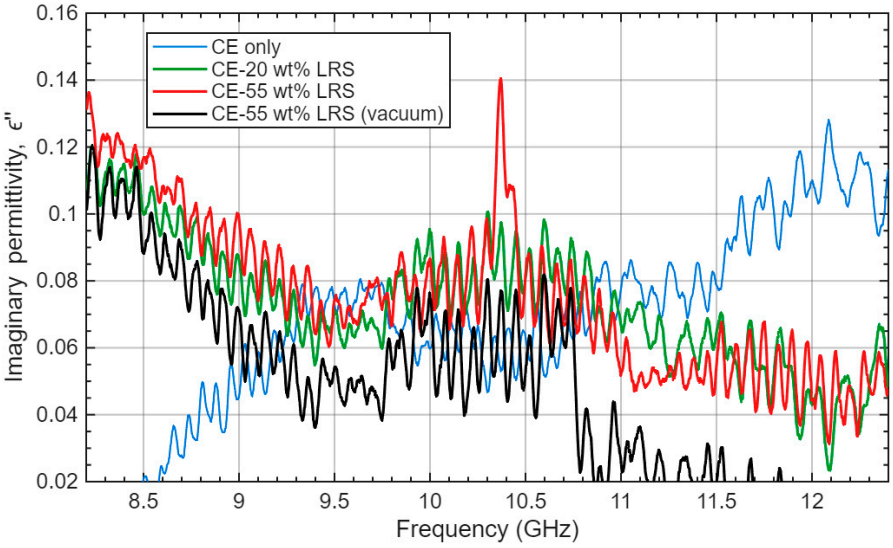
3.4. Electromagnetic Properties

For CE-LRS composites to function as electronic substrates, their electromagnetic properties must support predictable signal propagation while minimizing dielectric and magnetic losses. The real part of the permittivity (ε') determines the effective dielectric constant and therefore influences signal velocity and impedance. The imaginary part of the permittivity (ε'') and the dielectric loss tangent (tan δ), describe electromagnetic energy dissipation within the material. In addition, the relative permeability (μ'), should remain close to unity to avoid magnetic loss or unwanted magnetic dispersion during radio-frequency operation.

Figure 6 presents the frequency-dependent complex permittivity of neat CE resin and CE-OPRH4W30 composites with 20 wt% and 55 wt% LRS loading, including a vacuum-processed 55 wt% sample, measured across the X-band frequency range of 8.2–12.4 GHz. The corresponding X-band-averaged electromagnetic properties are summarized in Table 3.



(**a**)



(**b**)

Figure 6. (**a**) Frequency-dependent real permittivity (ε') and (**b**) frequency-dependent imaginary permittivity (ε'') of CE resin and CE-OPRH4W30 composites with 20 wt% and 55 wt% LRS loading, including the vacuum-processed 55 wt% LRS sample, measured across the X-band.

Table 3. Mean electromagnetic properties of CE resin and CE-OPRH4W30 composites across the X-band, including real (ε') & imaginary (ε''), parts of permittivity, loss tangent (tan δ), and relative permeability (μ').

Sample	ε'	ε''	tan δ	μ'
Only CE	3.10	0.0673	0.0217	~1
CE-20 wt% LRS	3.53	0.0737	0.0209	~1
CE-55 wt% LRS	4.38	0.0753	0.0172	~1
CE-55 wt% LRS (vacuum)	4.53	0.0754	0.0166	~1

For X-band waveguide measurements using the Nicolson–Ross–Weir algorithm, prior reports indicate typical uncertainties on the order of $\Delta\varepsilon' \approx 0.05$–$0.10$ for the real permittivity and $\Delta\varepsilon'' \approx 0.005$–$0.02$ for the imaginary permittivity [38]. These uncertainties arise primarily from sample-machining tolerances, residual air gaps between the specimen and the

waveguide walls, and calibration drift across the measured frequency band. Therefore, the differences in real part between the compositions in Table 3 are sufficiently large to support a clear compositional trend, while the smaller differences in ε'' should be interpreted as qualitative trends rather than precise quantitative changes.

The real permittivity (ε') increases systematically with LRS loading. This monotonic increase is expected because the silicate-rich LRS phase has a higher effective permittivity than the polymer matrix [39,40]. Across the measured X-band range, ε' remains nearly frequency-independent for all compositions, indicating stable dielectric behavior over the tested bandwidth. Such frequency stability is desirable for RF substrate applications because it supports predictable impedance and signal propagation across the operating frequency range [38,41,42].

The imaginary permittivity remains low for all compositions and changes only slightly with LRS loading. The values are close in magnitude and partly within the expected uncertainty range of the measurement. Therefore, the imaginary permittivity should not be overinterpreted as showing a strong compositional dependence. However, the dielectric loss tangent decreases with increasing LRS loading. This decrease occurs because ε' increases more substantially than ε'', resulting in a lower fractional dielectric loss. These results indicate that the addition of LRS increases the dielectric constant without introducing substantial microwave loss in the X-band.

To provide a predictive estimate of composite permittivity as a function of LRS loading, the measured data were compared with the Maxwell–Garnett effective medium approximation. This model treats the LRS particles as dispersed inclusions within a continuous CE matrix and is commonly used to describe the effective dielectric properties of composite materials [29]. The Maxwell–Garnett equation was inverted using the measured permittivity of the ambient pressure-processed 55 wt% LRS composite, the measured CE permittivity, and the calculated LRS volume fraction. Using densities of ρCE = 1.20 g/cm^3 and ρLRS = 2.82 g/cm^3, the 20 wt% and 55 wt% LRS composites correspond to approximately 9.6 vol% and 34.2 vol% LRS, respectively. Within the Maxwell–Garnett framework, the effective LRS permittivity was estimated as $\varepsilon_{LRS} = 8.19 - j0.071$. The value falls within the range previously reported for X-band measurements of highland-type lunar regolith simulants such as EAC-1A and JSC-2A [39].

Using the extracted ε_{LRS} value, the Maxwell–Garnett model was then evaluated in the forward direction to estimate the effective composite permittivity over a broader range of LRS loadings. The resulting prediction is shown in Figure 7 together with the measured values for neat CE, 20 wt% LRS, and 55 wt% LRS composites. The 20 wt% LRS sample agrees closely with the predicted trend in ε', supporting the use of the model as a practical tool for estimating dielectric constant at intermediate filler loadings. For ε'', the 20 wt% data point lies slightly above the predicted value, but the offset is comparable to the expected NRW measurement uncertainty. Overall, the Maxwell–Garnett analysis provides a useful framework for tailoring CE-LRS composite permittivity through adjustment of regolith loading.

The relative permeability of all measured samples remains close to unity, with $\mu' \approx 1.0$ across the X-band. The imaginary component of permeability is negligible over the measured frequency range. This behavior indicates that the CE-OPRH4W30 composites are effectively non-magnetic, as expected for the highland-type simulant used in this study. The absence of measurable magnetic loss is beneficial for RF substrate applications because it minimizes additional attenuation mechanisms associated with magnetic dispersion.

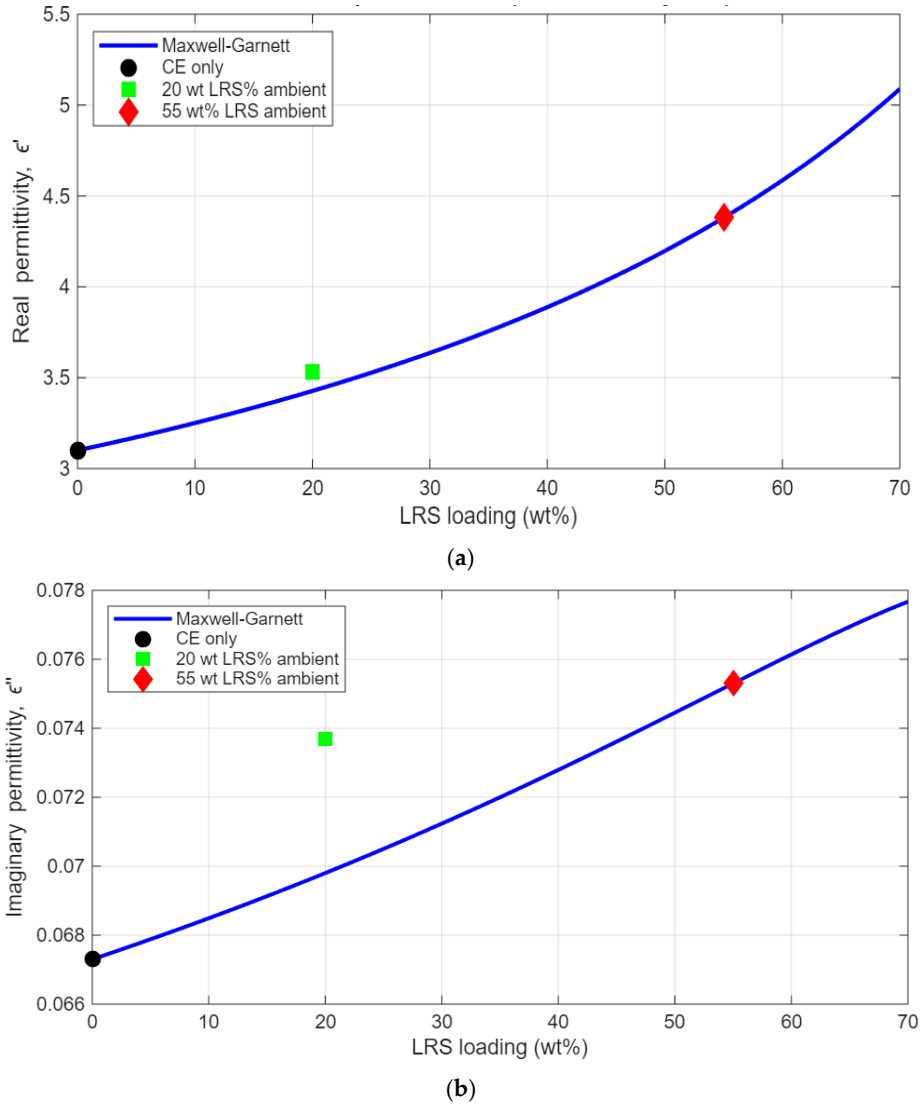


Figure 7. (**a**) Maxwell–Garnett (MG) effective medium prediction of (**a**) real and (**b**) imaginary effective permittivity of CE-LRS composites as a function of LRS loading (wt%), evaluated with ε_CE = 3.10 − j0.067 and the extracted ε_LRS = 8.19 − j0.071 (MG inversion of the 55 wt% ambient-cured sample). Measured points for the only CE, 20 wt% LRS, and 55 wt% LRS (ambient) samples are overlaid.

Overall, the CE-LRS composites exhibit a tunable dielectric constant, low dielectric loss tangent, frequency-stable permittivity across the X-band, and non-magnetic behavior. The electromagnetic response is also consistent with microstructural observations.

4. Conclusions

This study successfully developed and characterized a novel composite material system composed of LRS and CE resin, demonstrating its potential for manufacturing electronic substrates in space. The composite exhibits environmental stability. The high T_g of the cured CE resin (~230 °C) exceeds the maximum lunar temperature, ensuring thermal stability throughout lunar thermal cycles. The optimized vacuum-assisted curing process yielded a dense, well-integrated microstructure with low porosity (<1%), which is directly responsible for the high stiffness demonstrated by the DMA. The DMA revealed that vacuum processing enhances storage modulus and increases T_g through improved interfacial adhesion. The composite also presents favorable functional properties, with stable, low-loss dielectric performance and non-magnetic behavior suitable for circuit board

applications. While direct mechanical strength measurements (flexural, tensile) and long-term durability under combined lunar environmental conditions remain for future work, the CE-LRS composite represents a potential candidate for realizing ISRU for electronics. This work addresses the gap in polymer-based ISRU approaches by prioritizing environmental resilience over ease of processing. Unlike high-temperature sintering methods, our approach enables composite formation at lower processing temperatures, which preserves energy. Future research should focus on validating long-term durability under combined simulated lunar environments (vacuum, thermal cycling, radiation) and demonstrating the direct printing of circuits onto its surface.

Author Contributions: Conceptualization, R.L.O. and M.M.; methodology, B.M.A. and G.L.; validation, R.L.O., M.M., B.M.A. and G.L.; investigation, G.L. and B.M.A.; writing—original draft preparation, G.L. and B.M.A.; writing—review and editing, R.L.O. and M.M.; supervision, R.L.O. and M.M.; project administration, R.L.O. and M.M.; funding acquisition, R.L.O. and M.M. All authors have read and agreed to the published version of the manuscript.

Funding: This research was funded by NASA, grant number 80NSSC22M0250.

Data Availability Statement: The raw data supporting the conclusions of this article will be made available by the authors on request.

Acknowledgments: During the preparation of this manuscript, the author used DeepSeek-V2 for the purpose of language editing in the first draft. The authors have reviewed and edited the output and take full responsibility for the content of this publication.

Conflicts of Interest: The authors declare no conflicts of interest.

Abbreviations

The following abbreviations are used in this manuscript:

CE	cyanate ester
LRS	lunar regolith simulant

References

1. Ince, J.C.; Peerzada, M.; Mathews, L.D.; Pai, A.R.; Al-Qatatsheh, A.; Abbasi, S.; Yin, Y.; Hameed, N.; Duffy, A.R.; Lau, A.K. Overview of emerging hybrid and composite materials for space applications. *Adv. Compos. Hybrid Mater.* **2023**, *6*, 130. [CrossRef]
2. Suhaizan, M.S.; Tran, P.; Exner, A.; Falzon, B.G. Regolith sintering and 3D printing for lunar construction: An extensive review on recent progress. *Prog. Addit. Manuf.* **2024**, *9*, 1715–1736. [CrossRef]
3. Indyk, S.J.; Benaroya, H. A structural assessment of unrefined sintered lunar regolith simulant. *Acta Astronaut.* **2017**, *140*, 517–536. [CrossRef]
4. Faierson, E.J.; Logan, K.V.; Stewart, B.K.; Hunt, M.P. Demonstration of concept for fabrication of lunar physical assets utilizing lunar regolith simulant and a geothermite reaction. *Acta Astronaut.* **2010**, *67*, 38–45. [CrossRef]
5. Montes, C.; Broussard, K.; Gongre, M.; Simicevic, N.; Mejia, J.; Tham, J.; Allouche, E.; Davis, G. Evaluation of lunar regolith geopolymer binder as a radioactive shielding material for space exploration applications. *Adv. Space Res.* **2015**, *56*, 1212–1221. [CrossRef]
6. Warren, P.; Raju, N.; Ebrahimi, H.; Krsmanovic, M.; Raghavan, S.; Kapat, J.; Ghosh, R. Effect of sintering temperature on microstructure and mechanical properties of molded Martian and Lunar regolith. *Ceram. Int.* **2022**, *48*, 35825–35833. [CrossRef]
7. Zhang, R.; Wang, T.; Wang, G. Review of Lunar Regolith Forming Technologies for In-Situ Manufacturing/Construction on the Lunar Surface. *Addit. Manuf. Front.* **2025**, *4*, 200238. [CrossRef]
8. Provis, J.L. Activating solution chemistry for geopolymers. In *Geopolymers*; Elsevier: Amsterdam, The Netherlands, 2009; pp. 50–71.
9. Pederson, F.; Ellersick, L.; Kim, H.-J. A review of lunar regolith based alkali activated materials and sintered regolith for use as a construction material. *Acta Astronaut.* **2025**, *232*, 502–515. [CrossRef]
10. Pastore, R.; Delfini, A.; Albano, M.; Vricella, A.; Marchetti, M.; Santoni, F.; Piergentili, F. Outgassing effect in polymeric composites exposed to space environment thermal-vacuum conditions. *Acta Astronaut.* **2020**, *170*, 466–471. [CrossRef]

11. Hinojosa, M.; Rodríguez, C.A.; Aldaco, J.A.; Morales-Castillo, J.; Leal, A.E.; Salinas, V. Study of the Thermomechanical Performance of FR-4 Laminates During the Reflow Process. *J. Mater. Eng. Perform.* **2019**, *28*, 6761–6770. [CrossRef]
12. Matetich, C.; Vold, J. Regolith-based polymer matrix composites for in situ material creation for long-term extraterrestrial missions. *J. Aerosp. Eng.* **2023**, *36*, 04022103. [CrossRef]
13. Jakus, A.E.; Koube, K.D.; Geisendorfer, N.R.; Shah, R.N. Robust and elastic lunar and martian structures from 3D-printed regolith inks. *Sci. Rep.* **2017**, *7*, 44931. [CrossRef]
14. Taylor, S.L.; Jakus, A.E.; Koube, K.D.; Ibeh, A.J.; Geisendorfer, N.R.; Shah, R.N.; Dunand, D.C. Sintering of micro-trusses created by extrusion-3D-printing of lunar regolith inks. *Acta Astronaut.* **2018**, *143*, 1–8. [CrossRef]
15. Goyal, S.; Cochran, E.W. Cyanate ester composites to improve thermal performance: A review. *Polym. Int.* **2022**, *71*, 583–589. [CrossRef]
16. Li, S.; Zhu, Y.; Wang, Y.; Wang, B.; Huang, Y.; Yu, T. Cyanate ester resin based composites with high toughness and low outgassing performances. *Compos. Commun.* **2021**, *23*, 100574. [CrossRef]
17. Moulishwar Reddy, A.; Kandasubramanian, B.; Rath, S.K. Cyanate ester blends and composites to improve dielectric, mechanical, and thermal performance for functional applications. *Polym. Bull.* **2024**, *81*, 3781–3836. [CrossRef]
18. Zaman, S.; Favela, S.; Herrera, N.E.; Gandara, A.; Molina, L.; Hassan, M.S.; Gomez, S.G.; Ramirez, J.E.M.; Mahmud, M.S.; Martinez, A.C. 3D printing of cyanate ester resins with interpenetration networks for enhanced thermal and mechanical properties. *J. Appl. Polym. Sci.* **2024**, *141*, e55423. [CrossRef]
19. Başaran, C.; Selli, N.T. Dielectric and Mechanical Properties of Cyanate Ester-Based Composites Embedded with Different Glass Powders. *Materials* **2026**, *19*, 902. [CrossRef]
20. Williams, J.P.; Paige, D.A.; Greenhagen, B.T.; Sefton-Nash, E. The global surface temperatures of the Moon as measured by the Diviner Lunar Radiometer Experiment. *Icarus* **2017**, *283*, 300–325. [CrossRef]
21. John, B.; Reghunadhan Nair, C.P. 13-Syntactic Foams. In *Handbook of Thermoset Plastics*, 3rd ed.; Dodiuk, H., Goodman, S.H., Eds.; William Andrew Publishing: Boston, MA, USA, 2014; pp. 511–554.
22. Ren, X.; He, Z.; Wang, Z.; Pan, Z.; Qi, Y.; Han, S.; Yu, H.; Liu, J. Design, synthesis and properties of semi-alicyclic colorless and transparent polyimide films with high glass transition temperatures and low retardation for potential applications in flexible electronics. *Polymers* **2023**, *15*, 3408. [CrossRef]
23. Qiu, H.; Qiu, X.; Dai, X.; Sun, Z.-Y. Design of polyimides with targeted glass transition temperature using a graph neural network. *J. Mater. Chem. C* **2023**, *11*, 2930–2940. [CrossRef]
24. Luo, F.; Lin, C.; Jiao, L.; Du, Z.; Dong, Z.; Dai, X.; Duan, X.; Qiu, X. High glass transition temperature and ultra-low thermal expansion coefficient polyimide films containing rigid pyridine and bisbenzoxazole units. *J. Polym. Sci.* **2023**, *61*, 1289–1297. [CrossRef]
25. Wu, Y.; Chen, G.; Gao, L.; Zhang, W.; Li, S. Carborane-containing bismaleimide resins with excellent heat resistance and dimensional stability. *High Perform. Polym.* **2021**, *33*, 176–183. [CrossRef]
26. Feng, Y.; Sun, Q.; Guo, J.; Wang, C. High-performance bismaleimide resin with an ultralow coefficient of thermal expansion and high thermostability. *Macromolecules* **2024**, *57*, 1808–1818. [CrossRef]
27. Ning, Y.; Li, D.-S.; Jiang, L. Thermally stable and deformation-reversible eugenol-derived bismaleimide resin: Synthesis and structure-property relationships. *React. Funct. Polym.* **2022**, *173*, 105236. [CrossRef]
28. Cg, J.; Salunke, A.D.; Joshi, M.; Kandasubramanian, B.; Anand, A. Cyanate ester–epoxy blends toward microwave transparent polymer composites through resin film infusion for wideband electromagnetic applications. *Polym.-Plast. Technol. Mater.* **2022**, *61*, 145–160.
29. Sihvola, A.H. *Electromagnetic Mixing Formulas and Applications*; Iet: London, UK, 1999.
30. Ata, S.; Ono, T.; Kato, Y. Development of porous COP–ceramic composites for application as low-relative-permittivity, low-dielectric-loss substrates in next-generation communication systems. *Sci. Rep.* **2025**, *15*, 28001. [CrossRef]
31. Landel, R.F.; Nielsen, L.E. *Mechanical Properties of Polymers and Composites*; CRC Press: Boca Raton, FL, USA, 1993.
32. George, S.; Neelakantan, N.R.; Varughese, K.T.; Thomas, S. Dynamic mechanical properties of isotactic polypropylene/nitrile rubber blends: Effects of blend ratio, reactive compatibilization, and dynamic vulcanization. *J. Polym. Sci. Part B Polym. Phys.* **1997**, *35*, 2309–2327. [CrossRef]
33. Holsti-Miettinen, R.M.; Seppälä, J.V.; Ikkala, O.T.; Reima, I.T. Functionalized elastomeric compatibilizer in PA 6/PP blends and binary interactions between compatibilizer and polymer. *Polym. Eng. Sci.* **1994**, *34*, 395–404. [CrossRef]
34. Yang, Y.-K.; He, C.-E.; Peng, R.-G.; Baji, A.; Du, X.-S.; Huang, Y.-L.; Xie, X.-L.; Mai, Y.-W. Non-covalently modified graphene sheets by imidazolium ionic liquids for multifunctional polymer nanocomposites. *J. Mater. Chem.* **2012**, *22*, 5666–5675. [CrossRef]
35. Bindu, P.; Thomas, S. Viscoelastic behavior and reinforcement mechanism in rubber nanocomposites in the vicinity of spherical nanoparticles. *J. Phys. Chem. B* **2013**, *117*, 12632–12648. [CrossRef] [PubMed]
36. Sattar, M.A.; Patnaik, A. Role of interface structure and chain dynamics on the diverging glass transition behavior of SSBR-SiO_2-PIL elastomers. *ACS Omega* **2020**, *5*, 21191–21202. [CrossRef]

37. Chua, P.S. Dynamic mechanical analysis studies of the interphase. *Polym. Compos.* **1987**, *8*, 308–313. [CrossRef]
38. Yong, S.; Khilkevich, V.; Liu, Y.; Gao, H.; Hinaga, S.; De, S.; Padilla, D.; Yanagawa, D.; Drewniak, J. Dielectric loss tangent extraction using modal measurements and 2-D cross-sectional analysis for multilayer PCBs. *IEEE Trans. Electromagn. Compat.* **2020**, *62*, 1278–1292. [CrossRef]
39. Ramos Somolinos, D.; Plaza Gallardo, B.; Cidrás Estévez, J.; Stepanyan, N.; Cowley, A.; Auñón Marugán, A.; Poyatos Martínez, D. Electromagnetic characterization of EAC-1A and JSC-2A lunar regolith simulants. *Materials* **2024**, *17*, 3633. [CrossRef] [PubMed]
40. Tsubaki, S.; Fujii, S.; Yamamoto, M.; Kanamori, H.; Hoshino, T.; Hosoda, S.; Wada, Y. Self-sufficient production of lunar regolith gravels on the moon by ultrarapid microwave sintering. *ACS Omega* **2024**, *9*, 22488–22494. [CrossRef]
41. Sebastian, M.T.; Ubic, R.; Jantunen, H. Low-loss dielectric ceramic materials and their properties. *Int. Mater. Rev.* **2015**, *60*, 392–412. [CrossRef]
42. Coonrod, J. Understanding the variables of dielectric constant for PCB materials used at microwave frequencies. In Proceedings of the 2011 41st European Microwave Conference, Manchester, UK, 10–13 October 2011; pp. 938–944.

Disclaimer/Publisher's Note: The statements, opinions and data contained in all publications are solely those of the individual author(s) and contributor(s) and not of MDPI and/or the editor(s). MDPI and/or the editor(s) disclaim responsibility for any injury to people or property resulting from any ideas, methods, instructions or products referred to in the content.